Nanoscale

ROYAL SOCIETY OF CHEMISTRY

PAPER

View Article Online
View Journal | View Issue

Check for updates

Cite this: *Nanoscale*, 2023, **15**, 14439

Multi-layer core–shell metal oxide/nitride/carbon and its high-rate electroreduction of nitrate to ammonia†

Xiaoyu Li,‡[a] Ping Deng,‡[a] Mengqiu Xu,‡[a] Zhenbo Peng,[b] Yuhu Zhou,[a] Gan Jia,[a] Wei Ye, *[a] Peng Gao *[a] and Wei Wang *[a]

The electroreduction of nitrate to ammonia is both an alternative strategy to industrial Haber–Bosch ammonia synthesis and a prospective idea for changing waste (nitrate pollution of groundwater around the world) into valuable chemicals, but still hindered by its in-process strongly competitive hydrogen evolution reaction (HER), low ammonia conversion efficiency, and the absence of stability and sustainability. Considering the unique electronic structure of anti-perovskite structured Fe_4N, a tandem disproportionation reaction and nitridation–carbonation route for building a multi-layer core–shell oxide/nitride/C catalyst, such as $MoO_2/Fe_4N/C$, is designed and executed, in which abundant Fe–N active sites and rich phase interfaces are *in situ* formed for both suppressing HER and fast transport of electrons and reaction intermediates. As a result, the sample's NO_3RR conversion displays a very high NH_3 yield rate of up to 11.10 mol_{NH_3} $g_{cat.}^{-1}$ h^{-1} (1.67 mmol cm^{-2} h^{-1}) with a superior 99.3% faradaic efficiency and the highest half-cell energy efficiency of 30%, surpassing that of most previous reports. In addition, it is proved that the NO_3RR assisted by the $MoO_2/Fe_4N/C$ electrocatalyst can be carried out in 0.50–1.00 M KNO_3 electrolyte at a pH value of 6–14 for a long time. These results guide the rational design of highly active, selective, and durable electrocatalysts based on anti-perovskite Fe_4N for the NO_3RR.

Received 21st June 2023,
Accepted 11th August 2023

DOI: 10.1039/d3nr02972g

rsc.li/nanoscale

Published on 12 August 2023. Downloaded on 5/6/2026 3:11:28 AM.

[a]*College of Material, Chemistry and Chemical Engineering, Key Laboratory of Organosilicon Chemistry and Material Technology, Ministry of Education, Hangzhou Normal University, Hangzhou 311121, China. E-mail: yewei@hznu.edu.cn, gaopeng@hrbeu.edu.cn, wangwei2022@hznu.edu.cn*

[b]*Zhejiang Collaborative Innovation Center for High Value Utilization of Byproducts from Ethylene Project, Ningbo Polytechnic, Ningbo 315800, China*

†Electronic supplementary information (ESI) available. See DOI: https://doi.org/10.1039/d3nr02972g

‡These authors contributed equally to this work.

Wei Wang

Wei Wang is a lecturer at the College of Materials, Chemistry and Chemical Engineering, Hangzhou Normal University. He received his PhD degree from East China University of Science and Technology in 2020. His research interests are mainly focused on nanoscale materials and their application in photoelectrochemical energy conversion.

Introduction

Ammonia (NH_3) is an irreplaceable chemical raw material in human's manufacture and life, as the source material for nitrogen fertilizers, plastics, pharmaceuticals, explosives, synthetic fibers, resins and printing and dyeing.[1,2] According to statistics, the annual growth rate of ammonia production is expected to reach 40% by 2050 (>200 million tons). At present, the main technique adopted for ammonia production is the Haber–Bosch process (350–550 °C, 15–25 MPa), which has been recognized as an energy-intensive synthetic approach (consuming about 5.50 EJ per year) with a high carbon emission (450 million tons per year of CO_2).[3–5] Therefore, a new economical and environment-friendly strategy for ammonia production needs to be explored. In this backdrop, the production of ammonia from nitrate has been put on the table, which is based on the idea of changing waste (nitrate) into treasures (ammonia). It is known that nitrate pollution in groundwater has become a worldwide environmental problem and endangers people's health in a direct or indirect way, such as causing infants to suffer from methemoglobinemia. Recently, the theoretical feasibility of the production of ammonia from nitrate has been realized through an electrocatalysis reaction.[6,7] This direct 8-electron pathway (N^{5+} in nitrate to N^{3-} in ammonia) has a low equilibrium potential of 0.69 V

Published on 12 August 2023. Downloaded on 5/6/2026 3:11:28 AM.

versus the reversible hydrogen electrode (RHE) due to the weak N=O bond energy (204 kJ mol^{-1}) and effectively avoids the formation and re-cleavage of inert N≡N bonds (dissociation energy: 945 kJ mol^{-1}), which is obviously better than the ambient electrocatalytic N_2 reduction reaction (NRR).[8,9] In addition, N_2 has extremely low water solubility, resulting in a lower faradaic efficiency (FE) and ammonia yield in the NRR process. Comparatively speaking, the advantages in kinetics make the electrochemical nitrate reduction reaction (NO_3RR) a highly economical ammonia synthesis route.[10–12] Simultaneously, it should be stressed in particular that the 8-electron NO_3^--to-NH_3 process involves multiple intermediates, such as NO_2^-, NO^-, NO, *etc.*, implying that there are still challenges in optimizing the adsorption of multiple substances and accelerating the reaction.[13–15]

To compete with the Haber–Bosch process, further improvement in the yield of NH_3 (>1 mmol cm^{-2} h^{-1}) and a decrease of energy consumption are highly desirable. Recently, transition metal compounds have been intensively investigated in the NO_3^- reduction reaction (NO_3RR), including transition metal oxides (TMO), nitrides (TMN), carbides (TMC), and sulfides (TMS), because the metal centers in them with partial positive charge can effectively adsorb nitrate and nitrite anions while the partial negative charge centers, *i.e.*, nitrogen, are the proton-acceptor centers.[16–19] Iron-based nitrides with active Fe–N components on their surfaces exhibit an abnormally high conductivity (0.1–1.0 × 10^5 S cm^{-1}) and show enhanced electrocatalytic performance and durability for the NO_3RR. At the same time, it is also found that the Fe–N structure has a great influence on the catalytic activity of the electroreduction of nitric acid to ammonia.[20,21] In particular, anti-perovskite structured Fe_4N contains both Fe–N and Fe–Fe chemical bonds, resulting in its excellent metal conductivity and high spin polarizability.[22] However, the electrocatalyst with only a single active component is limited by the proportion relationship; the adsorption energy of the intermediate is linearly related and can't be optimized due to the high step-by-step catalytic selectivity.[23] Recently, it has been clearly demonstrated that the reaction rate and selectivity of a heterostructure catalyst system could be optimized by precisely tuning the proximity, hierarchy and content ratio of multiple active phases. Furthermore, it is also confirmed that the rationally designed heterostructures could modulate the catalyst's electronic structure to enhance the catalytic activity.[24,25] The ultimate aim of these tentative efforts is to regulate the proton and/or electron transfer, as well as the binding strengths of partially reduced intermediates adsorbed on transition metal centers. Another important problem in NO_3RR is the competitive side hydrogen evolution reaction (HER) under a low negative potential, resulting in a low NO_3RR faradaic efficiency. So far, it has been very challenging to improve the NO_3RR selectivity of the catalysts by restraining H_2 generation while maintaining a high NH_3 yield rate. In contrast to metal oxides, MoO_2 exhibits poor HER activity due to the inappropriate hydrogen adsorption, which is beneficial for the improvement of the faradaic efficiency.[26] In addition, it is also found that this HER can also be suppressed through compositing with other components, such as Mo^{6+}-rich MoO_2, which occasionally forms a passivation layer to prevent protons from transferring to the surface too quickly.[27,28]

Experimental

Synthesis of MFN nanospheres

0.11 g of $MoCl_5$ and an appropriate amount of $FeCl_2{\cdot}4H_2O$ were added to 10 mL of deionized water with different molar ratios (4 : 0, 4 : 1, 4 : 2, 4 : 3, 4 : 4). Then 0.3 g of NTA and 20 mL of isopropanol (IPA) were added and stirred until they were completely dissolved. After that the greenish solution was transferred to a 50 mL PTFE-lined stainless-steel autoclave and kept at 180 °C for 6 hours in an oven. After the reaction, the sample was adequately washed with distilled water and dried at 60 °C for 12 h. Finally, brown samples were collected and named MFN-*x* (*x* = 1, 2, 3, 4). The sample with a molar ratio of 4 : 0 was named MN.

Synthesis of MFC nanospheres

The as-prepared MFN-*x* and MN precursors were calcined in a quartz tube furnace at 550 °C under an Ar atmosphere for 2 hours. Finally, black powders were collected and named MFC-*x* (*x* = 1, 2, 3, 4) and MC.

Synthesis of FC (Fe/C) porous nanorods

The steps were consistent with those of MFC-2 only without $MoCl_5$ and the as-prepared sample was named FC.

Electrochemical nitrate reduction test

3 mg of catalyst was ultrasonically dispersed in a mixture of DI water (700 μL), isopropanol (250 μL) and Nafion (50 μL, 5 wt%) to form a catalyst ink. Then, the catalyst slurry (50 μL) was dropped onto a 1 × 1 cm^2 carbon paper (catalyst loading amount: 0.15 mg cm^{-2}). Then, it was dried naturally and used as a working electrode combined with an Ag/AgCl reference electrode and a Pt counter electrode, respectively. All nitrate reduction tests were performed using a three-electrode system in a H-type cell, in which the cathode chamber and anode chamber were separated by a commercial F117 membrane. The KOH and KNO_3 electrolyte was first bubbled with a continuous high purity Ar flow for 30 min. Then the nitrate reduction reaction was triggered by a fixed potential from −0.2 to −1.0 V *vs.* RHE for 1 h. The as-generated NH_3 in the cathode chamber was quantified by the colorimetric method and ^{1}H-NMR spectroscopy. The by-products of NO_2^-, H_2 and N_2 were determined and quantified by a colorimetric method and gas chromatography, respectively.

Results and discussion

Synthesis and structural characterization

The synthesis of the multilayer core shell MFC catalyst is shown in Scheme 1. Firstly, the micro-scaled core shell of MFN was obtained by a simple hydrothermal reaction, in which a

 This journal is © The Royal Society of Chemistry 2023

Published on 12 August 2023. Downloaded on 5/6/2026 3:11:28 AM.

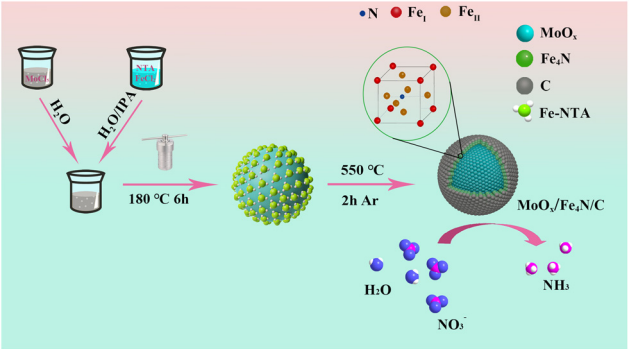

Scheme 1 A tandem disproportionation reaction ($Mo^{5+} \rightarrow Mo^{4+} + Mo^{6+}$) and nitridation–carbonation route (Fe_4N/C) for building a multi-layer core–shell MFC catalyst.

disproportionation reaction occurred: $2Mo^{5+} \rightarrow Mo^{4+} + Mo^{6+}$. As a result, Mo^{6+}-rich MoO_2 spherical particles were formed and uniformly coated with Fe-NTA. The MFN sample was first identified by XRD measurement (Fig. S1†), only the peaks at 26°, 36.8° and 53.5° corresponding to the (−111), (−211) and (211) crystal planes of MoO_2 (JCPDS: 32-0671) were identified, without any Fe-based compound. The composition was also confirmed by FT-IR examination. As shown in Fig. S2,† Mo═O, Fe–N and other typical chemical bands of NTA are depicted clearly. After comparison according to the field emission scanning electron microscopy (FE-SEM) measurement results (Fig. S3†), the MFN-2 sample with a molar ratio of $MoCl_5$ and $FeCl_2{\cdot}4H_2O$ of 4 : 2 was selected for the following synchronous nitriding carbonization treatment due to its homogeneous structure.

In order to realize the formation of a multi-layer core–shell oxide/nitride/C catalyst, the above prepared MFN-2 was first calcined at different temperatures from 400 to 650 °C with a 50 °C interval. As shown in Fig. S4,† after the reaction temperature was elevated up to 500 °C, three diffraction peaks of 24.7°, 33.5° and 42.8° corresponded to the (100), (110) and (111) crystal planes of anti-perovskite Fe_4N (JCPDS 86-0231) were identified, respectively, meaning that high temperature was conducive to the crystallization of Fe_4N. The following NO_3RR for NH_3 was first examined, as shown in Fig. S5,† in which the sample calcined at 550 °C displayed the most yield rate (11.10 mol_{NH_3} $g_{cat.}^{-1}$ h^{-1}). Therefore, all MFN precursors with different Fe salt additions ($MoCl_5 : FeCl_2$ = 4 : 0, 4 : 1, 4 : 2, 4 : 3, 4 : 4) were calcined at 550 °C, and the collected products were named MC, MFC-1, MFC-2, MFC-3 and MFC-4. Their morphologies and structures were characterized first by FE-SEM examinations. As shown in Fig. 1b and Fig. S6,† different from the spherical structure of MFC particles, FC particles display a rod-like structure composed of tiny grains (Fig. S7†). In addition, its XRD result (Fig. S8†) proves the metal Fe nature, not Fe_4N or MoO_2 presented in the MFC samples (Fig. 1a). This indicates that the suitable oxidizing environment around the Fe atom induced by MoO_2 is beneficial for lowering the energy barrier of Fe–N bond formation. Through comparing the FE-SEM images of the MFC samples shown in Fig. S6,† it is found that the spherical particles' surface becomes rougher with increased Fe salt addition, implying a grain growth. The exposed surface area of a catalyst is a critical factor to its catalytic performance. So the specific surface areas and pore diameters of the MFC samples were then investigated. As shown in Fig. S9 and Table S2,† the MFC-2 sample displays the largest area (76.2 m^2 g^{-1}) compared to others and a narrowly distributed pore size centered at 12 nm. The following catalytic measurements also confirm that MFC-2 has a best performance in NO_3RR, which inspires us to conduct a comprehensive and detailed investigation about it. In order to fully reveal its microstructure, MFC-2 was analyzed by high-resolution transmission electron microscopy (HRTEM). As shown in Fig. 1(d–g), the (−211) crystal face of MoO_2 (d = 2.43 Å), the (002) crystal face of carbon (d = 3.37 Å) and the (111) crystal face of anti-perovskite Fe_4N (d = 2.18 Å) were characterized from inside out, respectively. At the same time, a typical particle's selected area electron diffraction pattern (SAED) shown in Fig. 1h proves the existence of the crystalline MoO_2, C layer and Fe_4N again. The multi-layered core/shell structure was further identified by energy dispersive spectroscopy (EDS), as shown in Fig. 1i–s. It is seen that the Mo and O elements are mainly distributed inside, and the elements Fe, N and C are dispersed outside, which proves that the particles are composed of MoO_2, anti-perovskite Fe_4N and the carbon shell from inside out.

To further reveal the precise composition of MFC-2, X-ray absorption fine structure (XAFS) spectroscopy and X-ray absorption near edge structure (XANES) spectroscopy were conducted based on synchrotron radiation. As shown in Fig. 2a and b, a shoulder strap is located between 7114 eV of Fe_2O_3 and 7122 eV of Fe foil, which indicates that the oxidation state of Fe in Fe_4N is between 0 and +3. Their Fourier transforms based on the EXAFS spectra were then depicted, in which besides the Fe–Fe in Fe_4N, a specific peak at 1.41 Å was found, different from any peak in Fe_2O_3 or Fe foil, matched well with the reported bond length of Fe–N.[29,30] Furthermore, X-ray photoelectron spectroscopy (XPS) was applied to further determine its chemical states (Fig. S11†). The Mo 3d spectra of MFC-2 and MC (Fig. 2c) show peaks at binding energies of 229.5, 232.8, 234.2 and 235.9 eV, attributed to the signals of Mo^{4+} $3d_{5/2}$, Mo^{4+} $3d_{3/2}$, Mo^{6+} $3d_{5/2}$ and Mo^{6+} $3d_{3/2}$, respectively. The peak at 530.28 eV in the O 1s spectrum belongs to Mo═O, which is consistent with the above conclusion (Fig. 2d).[31,32] It is obvious that the disproportionation reaction ($MoCl_5 \rightarrow MoO_2 + Mo^{6+}$) expected by us has really occurred to form a Mo^{6+}-rich MoO_2 to suppress the HER. Fig. 2e shows the C 1s spectrum, in which the peak with a binding energy of 284.6 eV belongs to C–C, corresponding to the C shell formed after calcination.[33] As shown in Fig. 2f, the peak at 399.2 eV in the N 1s spectrum belongs to the Fe–N in Fe_4N (Fig. 2f).[34] Correspondingly, the Fe 2p spectrum shows multiple valence states in MFC (Fig. 2g), in which the peaks with binding energies of 707.8 and 720.4 eV belong to Fe^0, and the peaks with binding energies of 711.5 and 725.3 eV are due to Fe^{3+}. It is worth noting that Fe^0 and Fe^{3+} correspond to the Fe–Fe and

Published on 12 August 2023. Downloaded on 5/6/2026 3:11:28 AM.

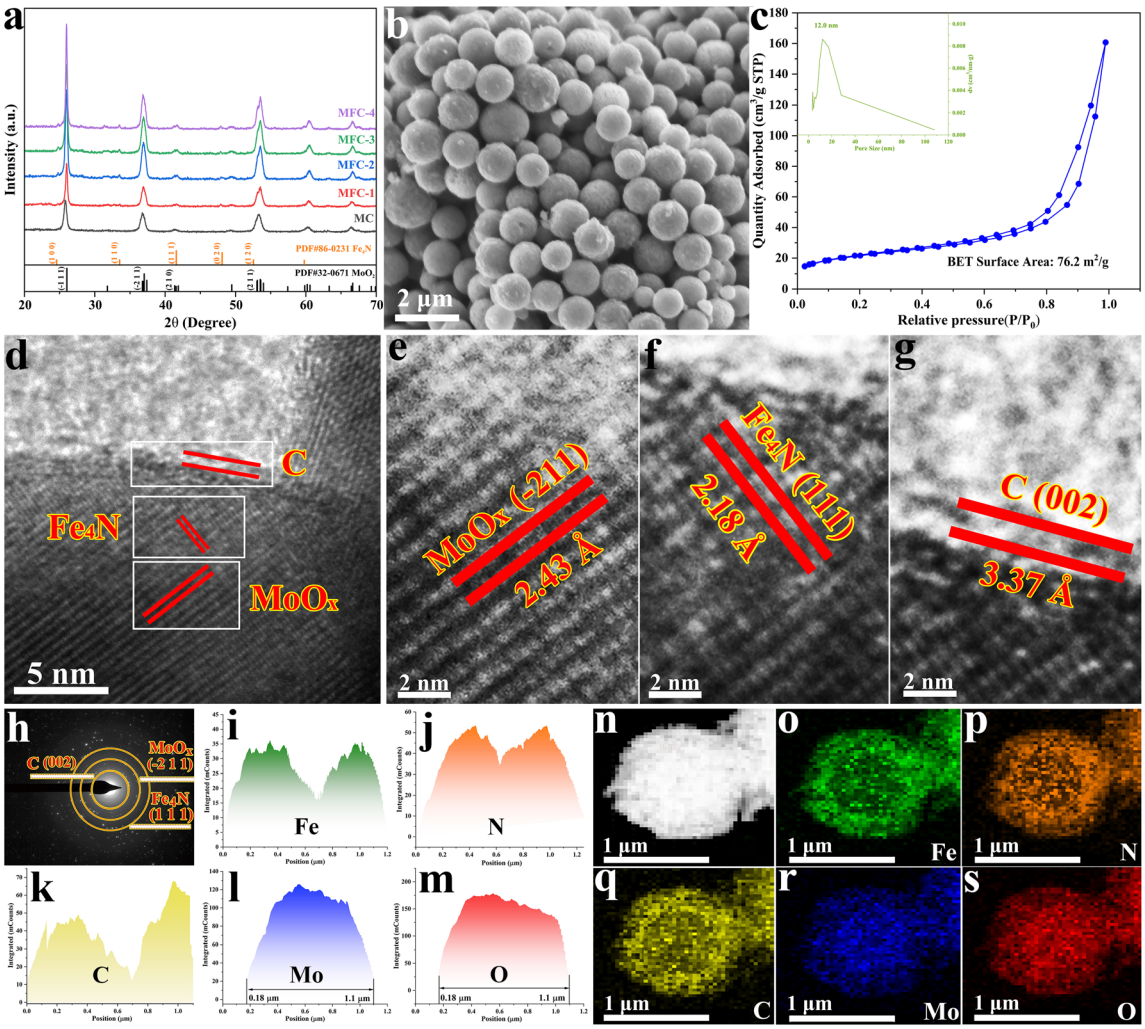

Fig. 1 Microstructure and composition characterization of the samples prepared with different Fe contents. MFC-2 is selected for detailed analysis because of its most excellent electrocatalytic activity. (a) XRD patterns of all the samples prepared with different Fe additions; (b) FE-SEM image of MFC-2; (c) N_2 adsorption–desorption isotherm and pore size distribution curve of MFC-2; (d–g) HRTEM images of MFC-2; (h) SAED image of MFC-2; (i–s) EDS element distribution diagrams of Fe, N, C, Mo and O in MFC-2.

Fe–N components in Fe_4N, respectively, which is significantly different from the Fe–O bond at 709–710 eV.[35,36] In order to further disclose the catalyst's composition, FT-IR spectral and Raman spectral measurements of the samples were conducted, respectively. As shown in Fig. 2h, the FT-IR spectrum results further confirm the existence of the Fe–N band appeared at 546 cm^{-1} for all catalysts except MC.[37,38] Meanwhile, the characteristic vibration of Mo═O at 936 cm^{-1} and the vibrations of O–H and C–C with wave numbers of 3432 cm^{-1} and 1620 cm^{-1} are also observed in all the samples.[39,40] In the Raman spectrum (Fig. 2i), the peaks at 195 cm^{-1} and 236 cm^{-1} are attributed to the bending vibration of Mo═O in MoO_2, some other peaks at 657 cm^{-1}, 819 cm^{-1}, 924 cm^{-1}, 991 cm^{-1}, 489 cm^{-1} and 661 cm^{-1} come from the stretching vibration of Mo═O in MoO_2. In addition, the bending vibration of Mo^{6+}═O was also observed at 281 cm^{-1} and 337 cm^{-1}, which proved the existence of Mo^{6+}.[41,42] At the same time, it is noted that Fe–N bonds with a trend of increasing strength are detected at 228 cm^{-1} and 360 cm^{-1} in the MFC samples due to the increased Fe element addition.[43] All the above results undoubtedly prove that the multi-layer core–shell MFC catalyst has been successfully prepared through a tandem disproportionation reaction and nitridation–carbonation route.

Electrochemical NO_3RR performance

The electrochemical NO_3RR performances of the above MFC and MC catalysts were investigated using H-type batteries with an electrolyte of 1 M KNO_3 and 1 M KOH, and all potentials were corrected *versus* the reversible hydrogen electrode (RHE), as shown in Fig. S12.† Their linear sweep voltammetry (LSV) curves are shown in Fig. S13,† which are quantified by Nessler reagent colorimetry (Fig. S14†). It is seen that once anti-perovskite Fe_4N is formed in the samples, all the current densities of the electrocatalytic NO_3RR are significantly increased at every

 This journal is © The Royal Society of Chemistry 2023

Published on 12 August 2023. Downloaded on 5/6/2026 3:11:28 AM.

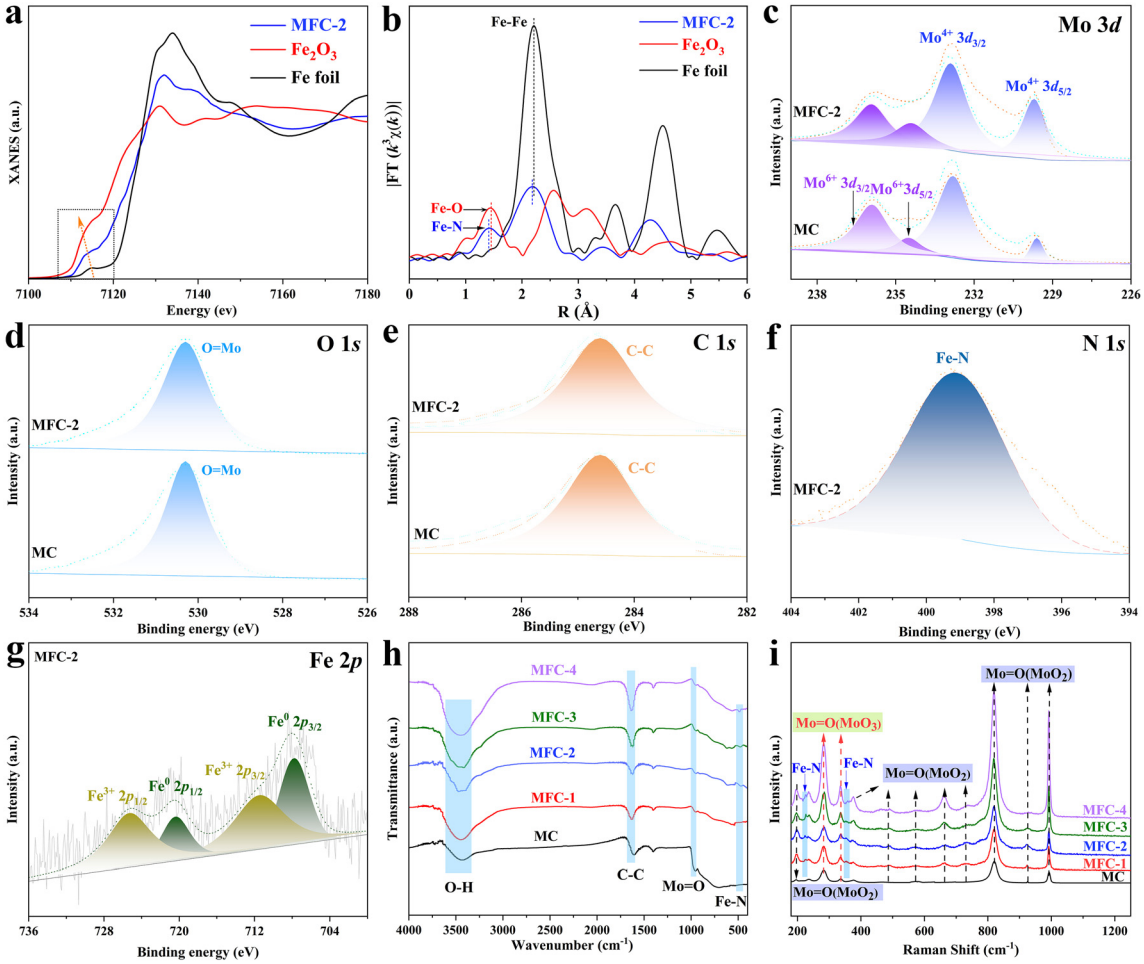

Fig. 2 Characterization of the compositions and chemical states of the as-obtained samples. (a) Normalized Fe K-edge XANES spectra of MFC-2 in reference to Fe foil and Fe_2O_3; (b) k_3-weighted Fourier-transform Fe K-edge EXAFS spectra; (c–g) XPS spectra of MC and MFC-2; (h) FT-IR spectra; (i) Raman spectra.

same voltage, proving the Fe_4N promoting effect. The recorded *I–t* curves also reflect this information (Fig. S15†), and the maximum current density at 1 V is 360 mA cm^{-2}. In order to confirm the fact that Fe in MFC is the critical electrocatalytic active site, LSV measurements of MFC-2 and MC in a mixture electrolyte of 1 M KNO_3, 1 M KOH and 1 M KSCN were conducted, as shown in Fig. S16.† It is obvious that after introducing SCN^- into the electrolyte to block the Fe^{3+} site, the LSV curve almost overlaps with the LSV curve of the MC sample, indicating that the Fe^{3+} site (not Fe^0) in anti-perovskite Fe_4N is indeed the critical active site for the NO_3RR. Fig. 3a shows the NH_3 yields and corresponding faradaic efficiencies of MFC and MC (Fig. S14†). It is found that the NH_3 yield of MFC-2 increases gradually as the voltage moves to a more negative region. At −1 V, the maximum NH_3 yield reaches 11.10 mol_{NH_3} $g_{cat.}^{-1}$ h^{-1} (1.67 mmol cm^{-2} h^{-1}). In sharp contrast, at −1.0 V, the highest NH_3 yields of MC, MFC-1 and MFC-3, MFC-4 samples are only 0.10, 7.04, 7.66, and 4.74 mol_{NH_3} $g_{cat.}^{-1}$ h^{-1}, respectively, which means that the NH_3 yield after Fe_4N formation is mostly elevated up to 115 times. Additionally, in the 0.1 M KOH and 0.1 M KNO_3 electrolyte, the ammonia yield reached 3.86 mol_{NH_3} $g_{cat.}^{-1}$ h^{-1} (0.58 mmol cm^{-2} h^{-1}), and the faradaic efficiency reached 74.4% at −1.0 V, greatly overpassing the previous literature. Importantly, it is worth noting that besides its very high ammonia yield, our sample also has a most excellent FE value compared with the previous literature to date (Fig. 3b and Table S3†), which indicates that the competitive HER is effectively inhibited at MFC, especially at a more negative potential (−0.5 to −1 V). The substantial increase in the NH_3 yield of MFC-2 proves that the Fe–N catalytic site in Fe_4N is really an ideal one for NO_3RR, especially after rational composition design. In addition, through etching the MoO_2 species of MFC-2 in a high concentration KOH (5 M) solution, pure Fe_4N was obtained to confirm the effect of MoO_2 on NO_3RR. It is seen in the XRD pattern (Fig. S17†) that the characteristic peaks of MoO_2 completely disappear. The following NO_3RR measurements indicate that the electrochemical Faraday efficiency decreased from 99.3% to 82.0% with a lowered ammonia production from 11.10 to 10.02 mol_{NH_3} $g_{cat.}^{-1}$ h^{-1} at −1.0 V. It is worth noting that the

Published on 12 August 2023. Downloaded on 5/6/2026 3:11:28 AM.

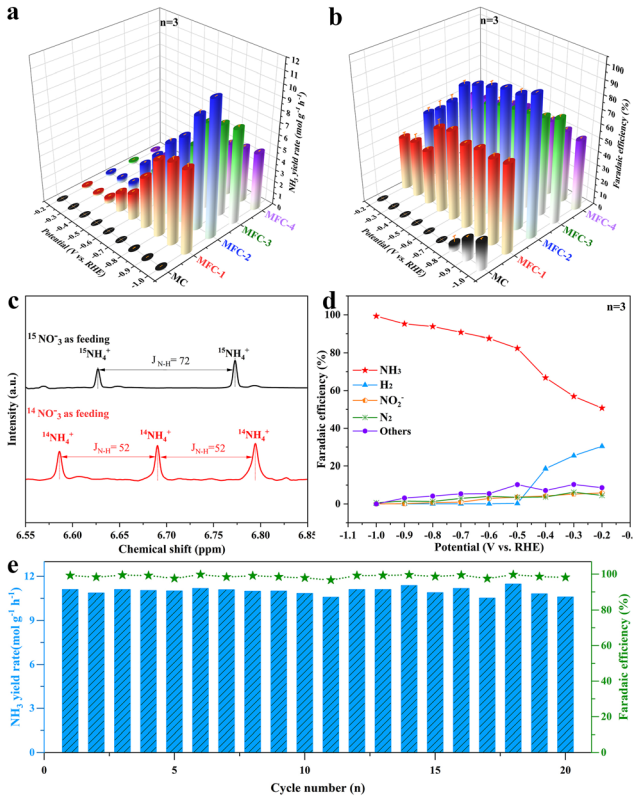

Fig. 3 (a) NH_3 yield rate; (b) the corresponding NO_3^--to-NH_3 faradaic efficiency of MFC-2 in reference to other samples; (c) ^{1}H-NMR spectra recorded in $^{14}NO_3^-$ or $^{15}NO_3^-$ solution; (d) potential dependent faradaic efficiencies of NH_3, NO_2^-, N_2 and H_2 for MFC-2; (e) cycling stability test of MFC-2 at −1.0 V in 1 M KNO_3 and 1 M KOH. (Data are presented as the mean values ± standard deviation derived from n = 3 independent experiments.)

Faraday efficiency of H_2 increased significantly (13.24%) compared with that before etching (0.04%). This phenomenon further proves that MoO_2 species are the main force to inhibit the side reaction of HER, and Fe_4N is the critical catalytic center for NO_3RR. In order to further confirm that the generated NH_3 really comes from the reduction of NO_3^-, ^{15}N isotope labelling experiments were carried out. As shown in Fig. 3c, the ^{1}H-NMR spectrum recorded in $^{14}NO_3^-$ shows a triplet mode with a coupling constant of J_{N-H} = 52 Hz, which can be specified as standard NH_4Cl. When $^{15}NO_3^-$ is used as a N source, a dipole pattern with coupling constant J_{N-H} = 72 Hz is detected, which is attributed to $^{15}NH_4^+$.[44] The possible by-products (NO_2^-, N_2 and H_2) in the NO_3RR are also quantified by Griess reagent colorimetry and gas chromatography (GC), as shown in Fig. S19–S21.† As shown in Fig. 3d, the H_2 FE of MFC-2 is 30.4% at −0.2 V and gradually drops to near zero once over −0.5 V. Simultaneously, the FE values of N_2 and NO_2^- are also lowered over −0.5 V, indicating that the MFC samples have good NH_3 selectivity under suitable potential. To reveal the widespread applicability of MFC in NO_3RR, we further evaluated the performance of MFC-2 under different NO_3^- concentrations and pH environments (Fig. S22 and S23†). The results showed that NO_3RR had higher NH_3 yield and faradaic efficiency under high nitrate concentrations (0.5–1.0 M) and pH environments (pH = 7–14). Besides the above measurements, stability tests were also carried out. Fig. 3e shows the cycling stability of durable MFC-2, in which it is seen that the MFC-2 sample can last for 20 consecutive cycles without obvious NH_3 yield and faradaic efficiency degradation. After 20 cycles (20 hours) of tests, the structure of MFC-2 (Fig. S25†) remained unchanged, thanks to the protection of a carbon layer under such a strong alkaline environment.[45] The XRD and XPS results of $MoO_2/Fe_4N/C$ after the electrocatalytic test, as shown in Fig. S26 and S27,† reveal that there is no evidence of structure and phase transformation appeared in the sample after the durability test, which further proves that the catalyst has excellent composition and structural stability in the long-term electrochemical process. In view of the excellent NO_3RR activity and stability of the MFC-2 sample, we can look forward with optimism that it has broad application prospects in future industrial catalysis.

Electrocatalytic mechanism

It is worth noting that, through investigation, this is the high ammonia output so far (Fig. 4a). In view of the excellent electro catalytic performance of MFC-2, we further evaluated its durability (Fig. 4b). After continuous testing for 50 hours, its current density has no significant change, which indicates its excellent stability. Electrochemical impedance spectroscopy (EIS) (Fig. 4c) shows that with the increasing Fe content, the samples' charge transfer resistances are obviously decreased due to the high conductivity of Fe_4N (~1.0×10^5 S cm^{-1}). Though MFC-4 has the smallest electrochemical impedance, this also makes its corresponding faradaic efficiency lowered. In contrast, the appropriate electrochemical impedance of MFC-2 effectively suppresses the side reactions with a high performance, and the faradaic efficiency reaches nearly 100%. According to previous research, there are five possible pathways for the NO_3RR on Fe-based catalysts (see the ESI† for details).[46,47] In order to further explore the inherent activity of the catalyst, the electrochemical active surface area (ECSA) of the catalyst was measured using a double-layer capacitance (C_{dl}) measurement method. As shown in Fig. S28,† the C_{dl} of MFC-2 (4.17 mF cm^{-2}) showed no significant change compared to that of MC (3.85 mF cm^{-2}), indicating that the greatly enhanced electrochemical performance of MFC-2 samples should be due to the higher intrinsic activity of Fe_4N, rather than the ECSA. To analyze the NO_3RR mechanism of MFC, we carried out *in situ* Raman measurements of MFC-2 and MC on rotating ring disk glassy carbon electrodes using a mixture of 1 M potassium nitrate and 1 M potassium hydroxide as the electrolyte, as shown in Fig. S29.† Firstly, in the *in situ* Raman spectrum of MC under a continuously regulated voltage from 0 to −1 V, it is found that no intermediates related to NO_3RR are detected between 0 V and −0.7 V except the peaks related to the catalyst and nitrate, which agrees with the NH_3 yield results under different potentials shown in Fig. 3a. Once the potential is scanned up to −0.8 V, the bending vibration peak

 This journal is © The Royal Society of Chemistry 2023

Published on 12 August 2023. Downloaded on 5/6/2026 3:11:28 AM.

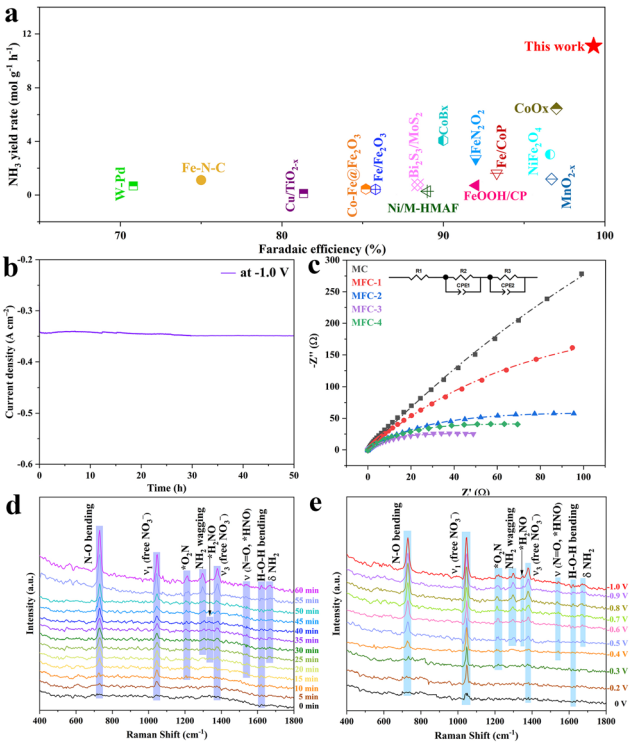

Fig. 4 (a) Comparation of ammonia yields reported in the literature and in this work; (b) current stability of MFC-2 tested at −0.1 V potential for 50 h; (c) EIS Nyquist plots of MFC-*X* and MC samples; (d) electrochemical *in situ* Raman spectra of MFC-2 in the range of 0–60 min; (e) electrochemical *in situ* Raman spectra of MFC-2 in the range of 0–1.0 V.

of NH_3 appears at 1298 cm^{-1} though the signal is relatively weak.[48] Due to the low concentration or nonexistence of intermediates, no signal of related intermediates is detected, which further confirms that MC is not the critical active site for the NO_3RR. As shown in Fig. 4d, *in situ* Raman spectra were recorded at −1.0 V with different reaction times to reveal this electrocatalytic dynamic mechanism. The vibration peaks at 730, 1047 and 1380 cm^{-1} are attributed to the bending mode of N–O (NO_3^-) and free NO_3^-, respectively. Obviously, with the reaction time extended from 0 to 60 minutes, the intensity of the vibration peak gradually increases, indicating that NO_3^- and intermediates are aggregated on the catalyst. In addition, the two vibration peaks at 1218 and 1548 cm^{-1} appeared at 10 and 15 min, respectively, corresponding to adsorbed NO_2 (expressed as $^-{*}O_2N$) and adsorbed HNO (expressed as the N=O stretching mode of *HNO species). The appearance of these two intermediate species indicates that NO_3^- is first transformed into $*NO_2$, and then into *HNO. As an important intermediate species, the peaks of $*H_2NO$ appears at 1322 cm^{-1} until 20 minutes, meaning that *HNO was further transformed into $*H_2NO$. The conversion of *HNO to $*H_2NO$ is a characteristic process of pathway 1 (see the ESI†).[49,50] In addition, the swinging mode (1298 cm^{-1}) and bending mode (1664 cm^{-1}) of NH_2 were observed at 25 minutes, indicating the formation of ammonia. The H–O–H bending mode at 1620 cm^{-1} also increases with the extended reaction time, implying that that the NO_3RR is assisted by proton coupling.[51] Then, in order to explore the thermodynamic mechanism, *in situ* Raman tests were carried out from −0.2 to −1.0 V potentials. As shown in Fig. 4e, the H–O–H bending pattern at 1620 cm^{-1} also increases with the negative shift of voltage, indicating that the NO_3RR is assisted by proton coupling. Between 0 and −0.2 V, vibrational peaks appear at 730, 1047 and 1380 cm^{-1}, attributed to the bending mode of N–O and the ν_1 and ν_3 modes of freely adsorbed NO_3^-, respectively. With a negative voltage shift to −0.3 V, the signal of adsorbed NO_2 (denoted as $^-{*}O_2N$) appears at 1218 cm^{-1}, indicating the conversion of NO_3^- to NO_2, followed by adsorbed HNO (denoted as the N=O stretching mode of *HNO species) emerged at 1548 cm^{-1} at −0.4 V, indicating the further conversion of $^-{*}O_2N$ to *HNO. When the voltage is further negatively shifted to −0.5 V, the characteristic peaks of $*H_2NO$ intermediate species as well as the oscillatory and bending modes of NH_2 are observed simultaneously at 1322 cm^{-1}, 1298 cm^{-1} and 1664 cm^{-1}, indicating the formation of ammonia. It is worth noting that the conversion of *HNO to $*H_2NO$ is the pathway 1 characteristic process (see the ESI†), again confirming the reaction course as follows:

$$* + NO_3^- + H^+ = * + HNO_3$$

$$* + HNO_3 + H^+ + e^- = *NO_2 + H_2O$$

$$*NO_2 + H^+ + e^- = *HNO_2$$

$$*HNO_2 + H^+ + e^- = *NO + H_2O$$

$$*NO + H^+ + e^- = *HNO$$

$$*HNO + H^+ + e^- = *H_2NO$$

$$*H_2NO + H^+ + e^- = *H_2NOH$$

$$*H_2NOH + H^+ + e^- = *NH_2 + H_2O$$

$$*NH_2 + H^+ + e^- = * + NH_3$$

Conclusions

This paper reports a tandem disproportionation reaction and nitridation–carbonation route for building an anti-perovskite Fe_4N-based multi-layer oxide/nitride/C catalyst, which enables the *in situ* formation of abundant active sites and rich phase interfaces for both fast transport of reaction intermediates and suppressing HER. After detailed examinations, it is proved that Fe–N in Fe_4N is the active site for the NO_3RR and the existence of MoO_2 can effectively suppress the HER side reaction. As a result, the sample's NO_3RR conversion displays a NH_3 yield rate of 11.10 mol_{NH_3} $g_{cat.}^{-1}$ h^{-1} (1.67 mmol cm^{-2} h^{-1}) with a 99.3% faradaic efficiency, and the highest half-cell energy efficiency of 30%. This study provides a new idea for constructing efficient and stable catalysts based on anti-perovskite Fe_4N, which has multiple electrochemical and catalytic properties.

Published on 12 August 2023. Downloaded on 5/6/2026 3:11:28 AM.

Author contributions

P. Gao, X. Y. Li and P. Deng conceived the idea and designed and performed the experiments as well as data analysis. M. Q. Xu performed the *in situ* Raman spectroscopy test and helped in analyzing the electrocatalytic mechanism. Z. B. Peng and Y. H. Zhou assisted with the materials synthesis, characterization, and the electrochemical performance test. P. Gao and X. Y. Li co-wrote the manuscript. P. Gao, W. Wang, W. Ye and G. Jia performed the analysis, supervised, and supported the work.

Conflicts of interest

The authors declare no competing interests.

Acknowledgements

This work was supported by the Innovation and Entrepreneurship Project of High-level Overseas Students in Hangzhou in 2021 (no. 4095C5021920466), the Medical Health Science and Technology Project of Zhejiang Provincial Health Commission (2023KY1009), Innovative Leading Talents in Colleges and Universities of Zhejiang Province and the Open Project of Key Laboratory of Superlight Materials and Surface Technology of Ministry of Education of Harbin Engineering University.

Notes and references

1 J. Liang, Z. Li, L. Zhang, X. He, Y. Luo, D. Zheng, Y. Wang, T. Li, H. Yan, B. Ying, S. Sun, Q. Liu, M. S. Hamdy, B. Tang and X. Sun, *Chem*, 2023, **9**, 1768–1827.
2 X. Xu, L. Hu, Z. Li, L. Xie, S. Sun, L. Zhang, J. Li, Y. Luo, X. Yan, M. S. Hamdy, Q. Kong, X. Sun and Q. Liu, *Sustainable Energy Fuels*, 2022, **6**, 4130–4136.
3 X. Guo, H. Du, F. Qu and J. Li, *J. Mater. Chem. A*, 2019, **7**, 3531–3543.
4 J. Liu, W. Kong, Z. Jin, Y. Han, J. Sun, L. Ma, Y. Niu and Y. Xu, *J. Mater. Chem. A*, 2020, **8**, 19278–19282.
5 J. Liang, Q. Liu, A. A. Alshehri and X. Sun, *Nano Res. Energy*, 2022, **1**, e9120010.
6 I. Mukherjee and U. K. Singh, *Sci. Total Environ.*, 2021, **787**, 147657.
7 T. Zhu, Q. Chen, P. Liao, W. Duan, S. Liang, Z. Yan and C. Feng, *Small*, 2020, **16**, e2004526.
8 W. Song, L. Yue, X. Fan, Y. Luo, B. Ying, S. Sun, D. Zheng, Q. Liu, M. S. Hamdy and X. Sun, *Inorg. Chem. Front.*, 2023, **10**, 3489–3514.
9 Y. Xu, Y. Sheng, M. Wang, T. Ren, K. Shi, Z. Wang, X. Li, L. Wang and H. Wang, *J. Mater. Chem. A*, 2022, **10**, 16883–16890.
10 Y. Xu, Y. Wen, T. Ren, H. Yu, K. Deng, Z. Wang, X. Li, L. Wang and H. Wang, *Appl. Catal., B*, 2023, **320**, 12981.
11 Z. Li, J. Liang, Q. Liu, L. Xie, L. Zhang, Y. Ren, L. Yue, N. Li, B. Tang, A. A. Alshehri, M. S. Hamdy, Y. Luo, Q. Kong and X. Sun, *Mater. Today Phys.*, 2022, **23**, 100619.
12 X. He, Z. Li, J. Yao, K. Dong, X. Li, L. Hu, S. Sun, Z. Cai, D. Zheng, Y. Luo, B. Ying, M. S. Hamdy, L. Xie, Q. Liu and X. Sun, *iScience*, 2023, **26**, 107100.
13 Z. Wang, D. Richards and N. Singh, *Catal. Sci. Technol.*, 2021, **11**, 705–725.
14 M. Duca and M. T. M. Koper, *Energy Environ. Sci.*, 2012, **5**, 9726.
15 Z. Deng, C. Ma, X. Fan, Z. Li, Y. Luo, S. Sun, D. Zheng, Q. Liu, J. Du, Q. Lu, B. Zheng and X. Sun, *Mater. Today Phys.*, 2022, **28**, 100854.
16 Y. Wang, A. Xu, Z. Wang, L. Huang, J. Li, F. Li, J. Wicks, M. Luo, D. H. Nam, C. S. Tan, Y. Ding, J. Wu, Y. Lum, C. T. Dinh, D. Sinton, G. Zheng and E. H. Sargent, *J. Am. Chem. Soc.*, 2020, **142**, 5702–5708.
17 H. Wang, J. Li, K. Li, Y. Lin, J. Chen, L. Gao, V. Nicolosi, X. Xiao and J. M. Lee, *Chem. Soc. Rev.*, 2021, **50**, 1354–1390.
18 S. Wang, L. Li, Y. Shao, L. Zhang, Y. Li, Y. Wu and X. Hao, *Adv. Mater.*, 2019, **31**, e1806088.
19 T. Ren, Z. Yu, H. Yu, K. Deng, Z. Wang, X. Li, H. Wang, L. Wang and Y. Xu, *Appl. Catal., B*, 2022, **318**, 121805.
20 D. Malko, A. Kucernak and T. Lopes, *J. Am. Chem. Soc.*, 2016, **138**, 16056–16068.
21 G. Ye, K. Zhao, Z. He, R. Huang, Y. Liu and S. Liu, *ACS Sustainable Chem. Eng.*, 2018, **6**, 15624–15633.
22 H. K. Singh, I. Samathrakis, N. M. Fortunato, J. Zemen, C. Shen, O. Gutfleisch and H. Zhang, *npj Comput. Mater.*, 2021, **7**, s41524.
23 H. Zhu, L. Gu, D. Yu, Y. Sun, M. Wan, M. Zhang, L. Wang, L. Wang, W. Wu, J. Yao, M. Du and S. Guo, *Energy Environ. Sci.*, 2017, **10**, 321–330.
24 N. R. Singstock and C. B. Musgrave, *J. Am. Chem. Soc.*, 2022, **144**, 12800–12806.
25 C. G. Morales-Guio, E. R. Cave, S. A. Nitopi, J. T. Feaster, L. Wang, K. P. Kuhl, A. Jackson, N. C. Johnson, D. N. Abram, T. Hatsukade, C. Hahn and T. F. Jaramillo, *Nat. Catal.*, 2018, **1**, 764–771.
26 J. Wang, Y.-p. Liu, H. Zhang, D.-j. Huang and K. Chu, *Catal. Sci. Technol.*, 2019, **9**, 4248–4254.
27 Y. Wan, Z. Wang, J. Li and R. Lv, *ACS Nano*, 2022, **16**, 643–654.
28 A. Kumar, J. Lee, M. G. Kim, B. Debnath, X. Liu, Y. Hwang, Y. Wang, X. Shao, A. R. Jadhav, Y. Liu, H. Tuysuz and H. Lee, *ACS Nano*, 2022, **16**, 15297–15309.
29 W. Ye, S. Chen, Y. Lin, L. Yang, S. Chen, X. Zheng, Z. Qi, C. Wang, R. Long, M. Chen, J. Zhu, P. Gao, L. Song, J. Jiang and Y. Xiong, *Chem*, 2019, **5**, 2865–2878.
30 X. Ao, W. Zhang, Z. Li, L. Lv, Y. Ruan, H.-H. Wu, W.-H. Chiang, C. Wang, M. Liu and X. C. Zeng, *J. Mater. Chem. A*, 2019, **7**, 11792–11801.
31 T. Hu, M. Wang, C. Guo and C. M. Li, *J. Mater. Chem. A*, 2022, **10**, 8923–8931.
32 F. Rehman, S. Kwon, C. B. Musgrave, M. Tamtaji, W. A. Goddard and Z. Luo, *Nano Energy*, 2022, **103**, 107866.

 This journal is © The Royal Society of Chemistry 2023

Published on 12 August 2023. Downloaded on 5/6/2026 3:11:28 AM.

33 X. Yang, H. Wang, D. Y. W. Yu and A. L. Rogach, *Adv. Funct. Mater.*, 2018, **28**, 1706609.
34 W. Kiciński, S. Dyjak and W. Tokarz, *J. Power Sources*, 2021, **513**, 230537.
35 A. M. Demin, A. V. Mekhaev, A. A. Esin, D. K. Kuznetsov, P. S. Zelenovskiy, V. Y. Shur and V. P. Krasnov, *Appl. Surf. Sci.*, 2018, **440**, 1196–1203.
36 Y. Zhou, Z. Zhou, R. Shen, R. Ma, Q. Liu, G. Cao and J. Wang, *Energy Storage Mater.*, 2018, **13**, 189–198.
37 S. R. Hormozi Jangi and M. Akhond, *Microchem. J.*, 2020, **158**, 105328.
38 B. Liu, H. Zhao, J. Yang, J. Zhao, L. Yan, H. Song and L. Chou, *Microporous Mesoporous Mater.*, 2020, **293**, 109820.
39 J. Chen, K. Sun, Y. Zhang, D. Wu, Z. Jin, F. Xie, X. Zhao and X. Wang, *Anal. Bioanal. Chem.*, 2019, **411**, 2781–2791.
40 T. N. Rudneva, N. S. Emel'yanova and S. V. Kurmaz, *Chem. Pap.*, 2018, **73**, 95–104.
41 C. Gu, D. Li, S. Zeng, T. Jiang, X. Shen and H. Zhang, *Nanoscale*, 2021, **13**, 5620–5651.
42 M. A. Camacho-López, L. Escobar-Alarcón, M. Picquart, R. Arroyo, G. Córdoba and E. Haro-Poniatowski, *Opt. Mater.*, 2011, **33**, 480–484.
43 F. Liu, N. Yan, G. Zhu, Z. Liu, S. Ma, G. Xiang, S. Wang, X. Liu and W. Wang, *New J. Chem.*, 2021, **45**, 13004–13014.
44 J. Liu, M. S. Kelley, W. Wu, A. Banerjee, A. P. Douvalis, J. Wu, Y. Zhang, G. C. Schatz and M. G. Kanatzidis, *Proc. Natl. Acad. Sci. U. S. A.*, 2016, **113**, 5530–5535.
45 H. Guo, N. Youliwasi, L. Zhao, Y. Chai and C. Liu, *Appl. Surf. Sci.*, 2018, **435**, 237–246.
46 T. Ren, K. Ren, M. Wang, M. Liu, Z. Wang, H. Wang, X. Li, L. Wang and Y. Xu, *Chem. Eng. J.*, 2021, **426**, 130759.
47 Z. Y. Wu, M. Karamad, X. Yong, Q. Huang, D. A. Cullen, P. Zhu, C. Xia, Q. Xiao, M. Shakouri, F. Y. Chen, J. Y. T. Kim, Y. Xia, K. Heck, Y. Hu, M. S. Wong, Q. Li, I. Gates, S. Siahrostami and H. Wang, *Nat. Commun.*, 2021, **12**, 2870.
48 C. Byram, S. S. B. Moram, A. K. Shaik and V. R. Soma, *Chem. Phys. Lett.*, 2017, **685**, 103–107.
49 Y. Wang, C. Wang, M. Li, Y. Yu and B. Zhang, *Chem. Soc. Rev.*, 2021, **50**, 6720–6733.
50 F. Lei, K. Li, M. Yang, J. Yu, M. Xu, Y. Zhang, J. Xie, P. Hao, G. Cui and B. Tang, *Inorg. Chem. Front.*, 2022, **9**, 2734–2740.
51 Y. H. Wang, S. Zheng, W. M. Yang, R. Y. Zhou, Q. F. He, P. Radjenovic, J. C. Dong, S. Li, J. Zheng, Z. L. Yang, G. Attard, F. Pan, Z. Q. Tian and J. F. Li, *Nature*, 2021, **600**, 81–85.